Thrust and wake characterization in small, robust ultrasonic thrusters

Thrust and wake characterization in small, robust ultrasonic thrusters

A. C. H. Tan, and F. S. Hover
Massachusetts Institute of Technology
Department of Mechanical Engineering
Cambridge, MA 02139 USA

***Abstract*-Among the new technologies in marine robotics is the trend toward smaller, cheaper and highly maneuverable vehicles, which could operate in swarms and also in very narrow and cluttered environments. A key challenge for vehicles with characteristic length of tens of centimeters scale is propulsion, where the designer faces high complexity in small vehicular space, as well as fouling concerns. Toward this end, we review and characterize the ultrasonic thruster (UST), which may be an attractive alternative to rotary and biomimetic-type actuators. The UST is a piezoelectric transducer that generates high-power, high-frequency acoustic waves, to produce bulk fluid movement for propulsion. We have systematically measured thrust and flow characteristics for a 7mm-diameter transducer with a range of voltages and sinusoidal frequencies, and varying duty cycles for a rectangular source signal; further, we installed three transducers into a 21cm underwater vehicle prototype. The experimental results allow us to outline the major parameters and considerations in our small vehicle and infer the mission length and speed using the UST technology.**

I. INTRODUCTION

We describe here a novel paradigm in underwater propulsion which utilizes acoustics means to generate thrust. We refer to it as the ultrasonic thruster (UST), and define it as an underwater thrust actuator made from a piezoelectric transducer (PZT), excited by a high-voltage source signal in the megahertz. The acoustical energy transmitted into the fluid medium experiences considerable absorption which results in momentum flux losses, leading to a bulk net flow along the transducer axial direction, which is associated with thrust generation. The phenomenon of net flow from a high-intensity acoustic transmitter is also known as acoustic streaming.

This alternative thrusting technology is well suited for very small underwater vehicles (tens of centimeters scale), whose miniaturized propulsion system complexity can become a challenge, and whose propulsive efficiency is disproportionately exacerbated by water viscosity and sensitivity to surface roughness. Today's underwater vehicles predominantly employ rotary propellers for locomotion, and some "fish-like" propulsors in biomimicry actuation. Some of the more persistent problems faced by very small marine vehicles are biofouling, entanglement from drifting debris, as well as corrosion. We believe that the UST technology can bring important and novel attributes to marine robotic devices and systems operating in low Reynolds numbers. These include low cost and high robustness when applied at very small scale. The robustness is derived from the fact that it effectively has no moving parts, mounted flush with a flat watercraft surface, hence requires low maintenance. Another desirable attribute is the UST can achieve an average intensity of 132dB (re 1μPa), which is destructive to living tissues and hence the device will not biofoul – these are properties unavailable in the rotary and biomimetic propulsors in use today.

At the same time, there is also a recent surge in interest for small exploratory underwater "microrobots," or "pods," and large-scale collaborative swarm systems are gaining more traction in terms of low cost and practicality, in addition to the original intent of formation morphing flexibility and physical coverage [1]. There is also interest to operate in cluttered or confined environments such as inside a piping network or crowded underwater structures. Naval reconnaissance missions may soon involve the deployment of clusters of expendable (even biodegradable) underwater robots for hazardous missions such as mine-hunting or surveillance mapping [2-4]. Interestingly, in the medical front, capsule-sized endoscopic swimming microbots are an option considered for minimally invasive surgery compared to open surgery examinations [5].

In view of the above, we constructed a UST-based marine vehicle. The basic UST is manufactured using available commercially off-the-shelf (COTS) transducers costing only a few dollars, while more advanced actuators can also be constructed at similarly low cost. We perform exclusive transducer-only testing of thrust and wake characteristics. The vehicle, *Huygens*, is built to provide a miniaturized platform to support multi-objectives oceanographic tasks and possibly military missions, as we describe below.

The following sections lay out the theoretical background for thrust generation, its acoustic efficiency, and kinetic energy as a result of the streaming. We outline the major design considerations in constructing the UST and *Huygens*, such as the housing and materials selection, shaping of *Huygens*, instrumentation, and the experimental setup. The propulsive force produced by a UST appears sufficient for light loading on small watercrafts, given that the wetted surface area is smaller. Some important design considerations and the UST efficiency are also discussed together with the experimental results. Since the paper is mostly focused on the underlying UST

This research was supported by the Singapore National Research Foundation (NRF) through the Singapore-MIT Alliance for Research and Technology (SMART) Center, Environmental Sensing and Monitoring (CENSAM).

978-1-4244-4333-8/10/$25.00 ©2010 IEEE

technology, background flow or crossflow would be out of the scope of this work.

A. Thrust generation

The UST is made from a membrane actuator mounted in a specially designed waterproof housing, excited by an electrical source at ultrasonic frequency; the UST is generally applied underwater to generate thrust. For the purposes of this paper, we assume that the actuator is piezoelectric. In this section, we establish some background material on the UST concept to elucidate the major physics at work, and to make several definitions that are useful in describing our experimental results.

A mathematical treatment relating ultrasonic thrust force, T (N), to acoustic power, P_x, in the far-field is given by Allison [6], and shall be briefly reviewed here. Fig. 1 defines several variables for the transducer and the acoustic field where the acoustic energy transmits in the right semi-hemisphere, propagating perpendicularly through a cross-sectional surface area $dS = s^2 \sin\theta\, d\theta\, d\phi$ of a control volume $dV = s^2 \sin\theta\, d\theta\, d\phi\, ds$. The thrust experienced on the surface of the transducer is expressed as

$$T = \rho v_0^2 a^2 \pi \int_0^{\theta_1} \frac{J_1(ka\sin\theta)^2}{\sin\theta} d\theta \qquad (1)$$

where ρ (kg/m^3), v_o (m/s), a (m), k, β, and $J_1(\cdot)$ denote the fluid density, transducer surface velocity, radius of the transducer, wavenumber, sound absorption coefficient, and Bessel function of the first kind, respectively, and $\theta_1 = \sin^{-1}\frac{3.832}{ka}$ is the upper limit of the dominant ultrasonic beamwidth [7]. The relationship between the acoustic power along the transducer axial direction x and the ultrasonic thrust is given by a simple correlation, $P_x = cT$, where c (m/s) denotes the sound speed. As we verify below, this also means the thrust is considerably lower than would a rotary propulsor operating at the same power level.

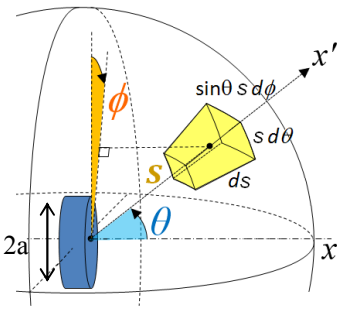

Figure 1. An elemental control volume in the far-field; the elevation angle, azimuth angle and distance from the center of transducer are θ, ϕ, and s respectively. The axial wake direction of the transducer is along the positive x-axis.

Finally, considering the electrical power loss inside the transducer, and accounting for the losses in converting the ultrasonic mechanical vibration to acoustics energy into the fluid, we introduce an acoustic efficiency factor η governing the thrust conversion. By relating the thrust production to the transducer voltage supplied, E, we obtain

$$T = \frac{\eta E_{rms}^2}{c\Re} \qquad (2)$$

where $\Re$ is the real component of the transducer impedance, and the electrical power, $P = \frac{E_{rms}^2}{\Re}$, corresponds to P_x at $s = 0$. This scaling of thrust with squared voltage will be used in Section III.

B. Acoustic streaming

Following Lighthill [8], acoustic streaming arises because of acoustic energy absorption along the path of propagation in a viscous, dissipative fluid medium. This loss in momentum flux across the control volume (Fig. 1) leads to a net force in the direction of the acoustic path. This net force in turn generates hydrodynamic flow in a steady state incompressible medium, as governed by the Navier-Stokes equation,

$$\rho \bar{u}_x \frac{\partial \bar{u}_x}{\partial x} = -\frac{\partial \bar{p}_0}{\partial x} + \mu \frac{\partial^2 \bar{u}_x}{\partial x^2} + F_x \qquad (3)$$

where $\bar{u}_x$ denotes the time-averaged streaming velocity along the x-axis, F_x is the radiation force along the x-axis, p_0 is defined as $p_0 = \rho c v_0$, and μ (kg/m·s) is the dynamic viscosity of the fluid. Since mass flow is conserved within the control volume, that is, $\rho \frac{\partial \bar{u}_x}{\partial x} = 0$, (3) can be solved by assuming $F_x = A e^{-\beta x}$ and using boundary conditions $\bar{u}_x(0) = 0, \bar{u}_x(\infty) = 0$, to obtain [9]

$$\bar{u}_x = \frac{A}{\nu\left(B^2 - \beta^2\right)}\left[e^{-\beta x} - e^{-Bx}\right] \qquad (4)$$

where A and B are characteristic coefficients of the fully developed axial velocity profile ($t \to \infty$), and ν is the kinematic viscosity $\nu = \mu/\rho$ (m^2/s), $\beta = 2\alpha$ for low intensity sound, and α (dB/m) is the absorption coefficient at a particular sound transmission frequency. Accordingly, Lighthill demonstrated that the radiation force can also be represented by the Reynolds stress along the axial direction:

$$\bar{F}' = -\frac{\partial \rho \bar{u}_x^2}{\partial x} \qquad (5)$$

In this case, it follows from (5) that $\overline{F}'$ is proportional to $\overline{u}_x^2$ and knowing that $\overline{F}'$ is also proportional to E^2, $\overline{u}_x$ is seen to scale directly with E.

Next, the total fluid discharge across the lateral section of the flow in Fig. 2 is given by $u_r\,\delta A = u_r 2\pi r\,\delta r$ (Fig. 3), and the mass flow rate through the elemental disc is $\rho u_r 2\pi r\,dr$. From [10] and later in the paper, it can be seen that the streaming field across a lateral section can be approximated by a Gaussian distribution of the following form, $u_r = u_x e^{-\frac{r^2}{2C^2}}$, where u_x (m/s) is the axial velocity in unit time, r (m) is the radial distance and C is a constant associated with the standard deviation of the Gaussian distribution. Hence the total kinetic energy of the velocity field in unit time from $x = 0$ to $x = x_f$, where x_f (m) is the focal distance from the flat transducer surface, is given by

$$\begin{aligned} K.E. &= \int_0^{x_f}\int_0^{R} \rho u_x u_r\, 2\pi r\, dr dx \\ &= 2\pi\rho \int_0^{x_f}\int_0^{R} u_x^2\, r\, e^{-\frac{r^2}{2C^2}}\, dr dx \end{aligned} \tag{6}$$

where R (m) is the radius of u_r (m/s) profile subtended by θ_l at x_f. Substituting (4) into (6), and solving the double integral, the total kinetic energy in unit time becomes

$$\begin{aligned} K.E. = \frac{\pi\rho A^2 C^2}{v^2\left(B^2-\beta^2\right)^2}\Bigg(&-\frac{1}{\beta}e^{-2\beta x_f} + \frac{1}{\beta+B}e^{-(\beta+B)x_f} - \\ &\frac{1}{B}e^{-2B x_f} + \frac{1}{\beta} - \frac{1}{\beta+B} + \frac{1}{B}\Bigg)\times\left(1 - e^{-\frac{R^2}{2C^2}}\right) \end{aligned} \tag{7}$$

While (7) sums up the total kinetic energy within the streaming field up to the focal distance, streaming at distances *above* x_f will evidently slow down, and free turbulence occurs due to the boundary between the stationary ambient water and the insonified flow – a process called entrainment. We consider regime $x > x_f$ to be no longer reliable or valid for *K.E.* calculation. Instead, (7) will be used in the later discussion to follow. Finally, it follows earlier that $\overline{u}_x$ scales directly with E and knowing that *K.E.* is also proportional to u_x^2 from (6), *K.E.* is seen to scale directly with E^2. This scaling of *K.E.* with square voltage will be used in Section III as well.

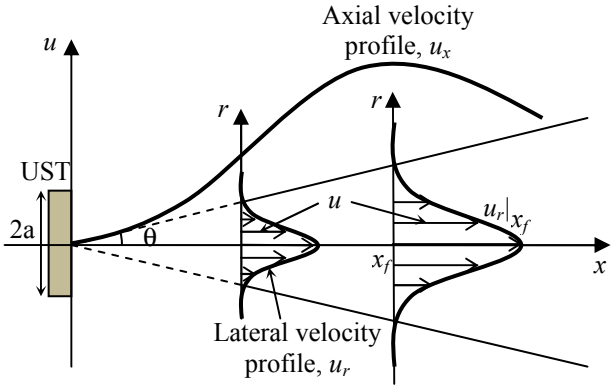

Figure 2. Velocity distribution of the acoustic streaming. Lateral velocity profile approximates a Gaussian distribution while axial velocity follows a rapid increase in velocity before a gradual decline.

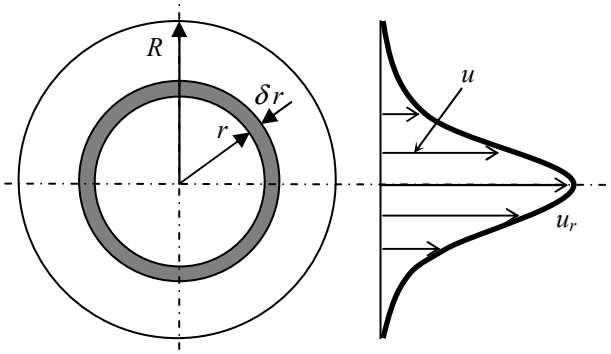

Figure 3. An elemental disc sectioned laterally from the ultrasonic field. The center of the circles is where the axis of the transducer passes through. The shaded annulus area, $2\pi r\,\delta r$, is an elemental area where flow discharges.

When the voltage at the transducer is very high, acoustic nonlinearity develops, enhancing the streaming velocity. In particular, weak shock theory [11] indicates that finite amplitude acoustic pressure waves will distort along the propagation path, becoming highly skewed and thus containing higher harmonics. These higher frequency components experience even more absorption in the fluid, resulting in a higher momentum flux gradient and so a higher streaming velocity. It has been reported that, qualitatively, this absorption increases without any change in viscosity μ [11]. Numerical simulations of the phenomenon were provided by Mitome *et al.* [12] and Wu and Du [13]; our experimental results, as detailed in Section III, are in agreement, as are those reported by Starritt *et al.* [14]. Once the distortion is maximized, that is, once the waveform takes a fully developed sawtooth shape, the velocity saturates.

II. EXPERIMENTAL SETUP

In this section, we characterize thrust and wake velocity for specific UST hardware, and then investigate in detail how these properties can be modified using different source signals; we vary voltage, frequency and waveform. We also developed an underwater vehicle prototype to demonstrate the ultrasonic propulsion capability.

A. Materials and methods

We use standard piezoelectric transducer technology for the conversion of electrical to acoustical energy. The transducer (Murata Manufacturing Co. Ltd) is made from a circular PZT plate measuring 7mm in diameter, housed in a 10mm diameter waterproof metallic casing; see Fig. 4. In our prototype vehicle described below, three USTs are connected to switches for actuation control, and 50Ω coaxial cables connect the three switches to a single power amplifier (ENI 3100L). When the ultrasonic transducer functions in a continuous wave (*cw*) mode, the thin metal housing provides excellent heat dissipation. Convection and acoustic streaming also aid in carrying away heat from the transducer surface [15].

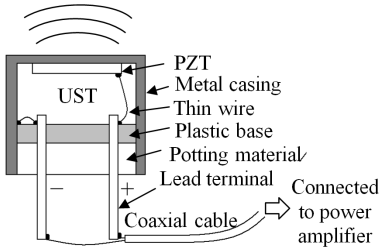

Figure 4. Construction of the UST (adapted from Murata Manufacturing Co. Ltd).

B. Source signals

To generate a source signal for the UST, a function generator is connected to the power amplifier. The ENI unit accepts an oscillatory input up to a maximum of $1V_{rms}$ ($2.8V_{pp}$), and amplifies at a gain of 50dB for a 50Ω output impedance. It is a Class A amplifier which means it will be unconditionally stable, and maintains linearity even with a combination of mismatched source and load impedance. We investigate a sinusoid source in the range of 1–8.5MHz and 0.2–$2.8V_{pp}$. We also consider the range 20–80% duty cycle using a square waveform.

C. Thrust force setup

The force measurement setup is summarized as follows. An ultrasound semi-anechoic tank measuring 1.2m×0.6 m×0.6 m is filled with distilled water and covered with an acrylic sheet, as shown in Fig. 5. In order to accurately measure the thrust produced by the UST, we developed an approach which allows sensitivity control by sliding the UST along an L-shaped arm. The moment is measured with a precision torque sensor. Other methods have been proposed for measuring these very fine-scale forces, for example, to attach and submerge a UST on one end of a vertical pendulum, hinged off-center, with the other end flexing a strain gauge [6]. Another approach is to attach the UST to a free-hanging wire and take photographs of the displacement as the UST is being actuated [16]. We found that the setup in Fig. 5 provides very good accuracy and repeatability, as indicated in the calibration plot of Fig. 6. The manufacturer's accuracy for the torque meter is ±0.09mN·m, and the effect of absolute error in the calibration thrust force averages about ±0.6mN, when our dial gauge is positioned 0.5m from the torque axis on the L-arm. Hence the total force uncertainty is around 0.8mN. Torque calibration is performed prior to all test sets. Thrust stabilizes and is recorded about ten seconds after turning on the power; then the power is turned off. We maintain a minimum of ten-second rest period between all tests, to allow for cooling and for the water to settle.

We note that measurements were made with three separate physical systems, located at MIT and at the SMART Center in Singapore, which have some differences in (megahertz) resonant behavior that could not be completely calibrated. For example, in Figs. 9, 12, and 14, the 50% duty cycle, the sinusoidal wave input leads to 11, 13.5, and 13mN of thrust, respectively. Unfortunately, the discrepancy is not entirely accounted for by different voltage levels at the transducer, although in some cases their levels are quite close. This said, we believe that each of the plots shown is self-consistent.

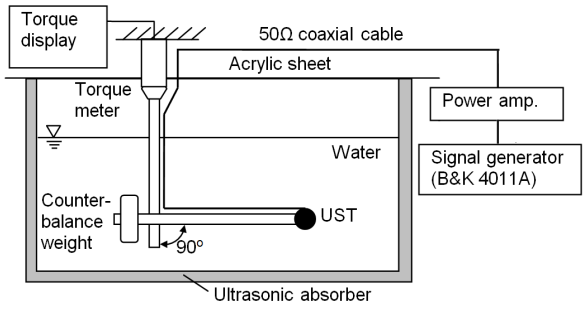

Figure 5. The semi-anechoic water tank and torque sensor used to measure UST thrust; thrust is generated in the direction perpendicular to the page.

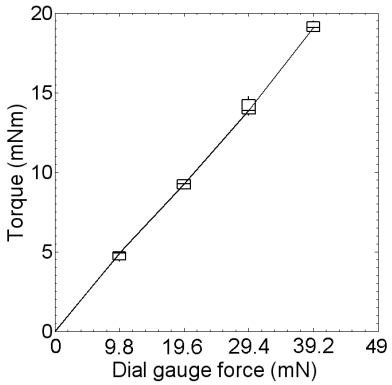

Figure 6. Calibration of the test rig. Each of the four points shown is an average of four separate force applications using a sensitive dial gauge.

D. Acoustic streaming measurement

Two-dimensional Digital Particle Image Velocimetry (DPIV) provides an accurate depiction of the UST wake, and beyond the entrainment boundary in the far-field. In similarly-scaled conditions, it has been reported that a 2% standard deviation at the point of maximum velocity can be expected with DPIV [17]; we found that a 5% error is achievable in comparing measured thrust with thrust calculated from the velocity field [10]. Our DPIV system is set up in a water tank measuring 2.4m×0.7m×0.7m, as shown in Fig. 7.

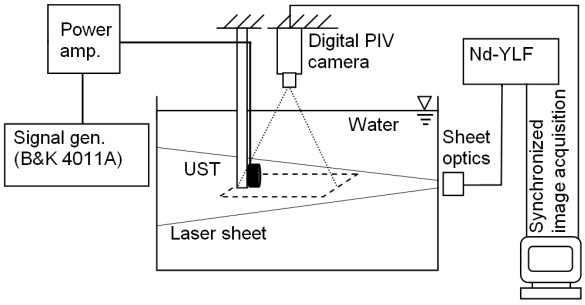

Figure 7. Schematic diagram of the DPIV tank setup. Acoustic streaming is illuminated by a laser sheet, and images are captured by a digital camera for post-processing.

A pulsed laser sheet, produced by a Quantronix diode pumped Q-switched frequency laser (Darwin-527-30M), spreads horizontally through the water tank, coincident with the UST's axial direction. The tank is seeded with 50μm polyamide particles, and a camera viewing the laser sheet perpendicularly traces the streaming particles when the UST is operating. The camera samples 300 timed, paired images at 400Hz, in a 0.2m×0.2m field of view. Post-processing is carried out using DaVis 7.1 software. The UST transducer is positioned at 1.2m from the sheet optics, 0.4 m from each adjacent tank wall, and 0.3m below the water surface. The time taken for the stream to become established has been reported variously at about 0.5s [18] and 20s [19]. We allow at least one minute of flow before the camera starts recording. Specific kinetic energy of the flow up to the focal distance x_f shown in the next section is the average of 150 measurements; recording the frames takes less than one second. Then the power is turned off, and the tank water is allowed to settle for at least one minute. This schedule is not the same as for thrust measurements, as the transducer is powered, and cools, for considerably longer time during DPIV tests.

Our note above about uncalibrated variations in power system resonant behavior holds for wake kinetic energy as well, and affects comparisons between Figs. 11, 13, and 15. The calculated particle velocities are subject to noise depending on the interrogation window size, the number of seeded particles, and the sampling rate, as well as other parameters. We made efforts to tune these for the lowest noise level.

E. Small underwater prototype, Huygens

We designed and constructed a small, streamlined shell with three embedded UST devices for propulsion and steering in the horizontal plane. The shell measures 215mm×160mm×80mm, profiled by a truncated NACA 0054 airfoil in the side view, and a truncated NACA 0025 airfoil in the plan view, as shown in Fig. 8. The shell is made from high-strength urethane foam for buoyancy, and coated with polyurethane. A UST is positioned at the rear end of the craft to provide forward thrust, and two USTs subtending 120° are symmetrically located on each side of the front end – at the "fish eyes" position. Together, these provide the right/left steering and backing thrust. Inside the shell, two rectangular cavities are machined, measuring 100mm×100mm×35mm, and 45mm×60mm×30mm. The shell can be opened into two halves via a stepped mid-section opening, lined with double O-rings for a watertight seal. The cylindrical UST seats are also lined with O-rings. The vent shown in the top left corner of Fig. 8 allows for a tether or an antenna for shallow-water wireless control.

For our preliminary vehicle speed measurements, we used a high resolution Vision Research digital camera (Phantom V10) mounted with a wide-angle 20mm lens from Sigma. We sampled the advance speed of *Huygens* at 40samples/second over a straight course of 0.6m; the craft was allowed to accelerate for ten seconds before beginning the velocity measurement. Although a tether was attached to the vehicle for these tests, we maintained a large loop hanging below the vehicle, and moved the top of the tether along with the vehicle, using a sliding car and post.

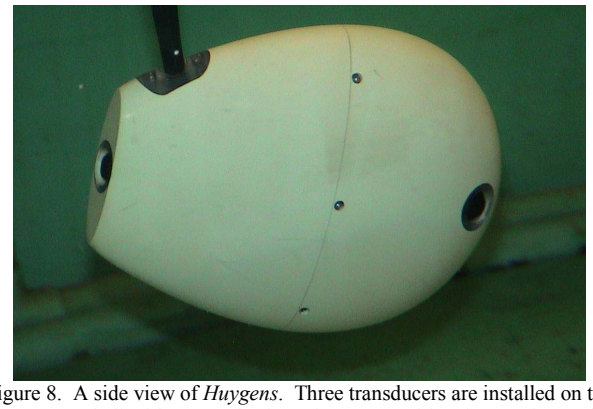

Figure 8. A side view of *Huygens*. Three transducers are installed on the *Huygens* shell with two at the frontal "eyes" position for steering and another in the rear for forward thrust. Tethered signal generates a multiplexed 7MHz sinusoidal input to the three USTs. A straight course advance speed of *Huygens* can go up to 5cm/s.

III. EXPERIMENTS WITH THE UST

Fig. 9 shows thrust force as a function of frequency, for a sinusoidal waveform. The thrust has obvious peaks near 11mN when operated at 7MHz, which can also be computed using the thickness mode frequency constant, $N_t = f_0\, h$, where h (m) is the thickness of the PZT, and $N_t = 1970$ as specified by the manufacturer. We will focus on this frequency in most of the discussion to follow. Fig. 10 illustrates the DPIV velocity field for a sinusoidal waveform at 7MHz, with amplified output voltage $54V_{rms}$. The maximum axial streaming velocity is observed at the point (0mm, 120mm) in the image, illustrating a fundamental feature of the UST – that *net fluid flow is zero at the transducer face*. Considering the same waveform configurations and frequencies as in Fig. 9, a similar peak at 7MHz in the total kinetic energy can be seen in Fig. 12.

Figs. 13 and 14 summarize our findings specifically at the 7MHz resonant point. Thrust generally increases with output voltage, but then starts to flatten out above the amplified output voltage of $60V_{rms}$. From Fig. 12 and from (2), the scaled thrust level of the sinusoidal signal is $3.8\times10^{-3}mN/V^2$ at $59V_{rms}$. Scaled thrust decreases gradually as the output voltage increases, and the absolute thrust appears to saturate above $60V_{rms}$ – a result also reported in another publication [15]. The kinetic energy points in Fig. 13 show similar trend as well. Using the *K.E.*-E^2 proportionality relationship from Section

I(B), the scaled kinetic energy at $54V_{rms}$ is calculated to be $1.5\times10^{-7}W/V^2$ respectively.

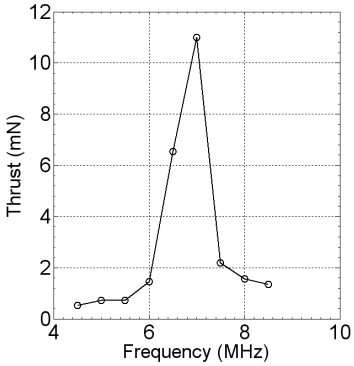

Figure 9. Measured thrust versus source frequency for sinusoidal waveforms supplied at $59V_{rms}$.

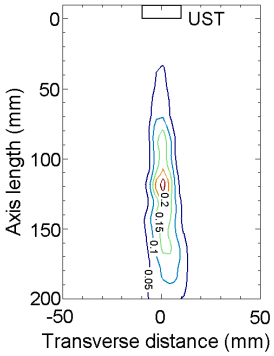

Figure 10. DPIV velocity field contours generated with a sinusoidal source at 7MHz and 54Vrms with each velocity contour step at 0.05m/s interval. A focal point can be clearly seen at (0mm, 120mm).

Although increasing the output voltage always increases thrust, the wake velocity of the sinusoidal source appears to saturate near $55V_{rms}$. The phenomenon of saturation can be explained by distortion in finite-amplitude traveling waves, according to weak shock theory as mentioned earlier. On the other hand, the fact that thrust in this case increases with input power despite the saturation of velocity highlights our earlier comment that the thrust production mechanism involves the wake only indirectly, and in a manner that is distinct from other propulsors. This fact may offer some interesting avenues for UST design, where the wake and the thrust force could be manipulated independently. This is especially useful in a scenario where larger thrust is desired but the wake has to be weak at the same time, for example, to minimize stirring up particulates near the seabed.

Considering variations in the duty cycle using a square waveform, Fig. 14 shows that the waveform generally maintains a higher dimensional thrust level near 50% duty cycle, preserving an almost symmetrical inverted-U profile between 20% and 80% duty cycle, as might be expected. At 50% duty cycle, thrust is observed to be around 12.8mN. Scaling thrust with the corresponding output voltage, the same profile is still noticeable but with a skew centered at 60% duty cycle, suggesting a slight advantage in thrust production at that regime. Fig. 15 shows similar properties for the total kinetic energy.

Summarizing, increasing the output voltage of the power amplifier will no doubt increase the thrust and kinetic energy production of the sinusoidal waveform, but at the same time, introduces a disproportionate relationship [15]. We also see that using square waveform at different duty cycles can bring out other characteristics, which can be useful for UST design considerations.

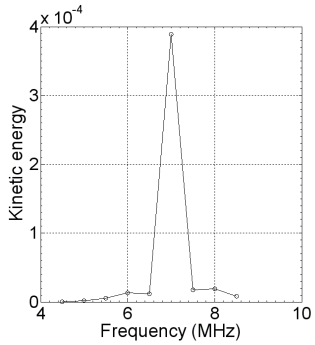

Figure 11. Total kinetic energy versus source frequency, from DPIV. The sinusoidal signal is supplied at $54V_{rms}$.

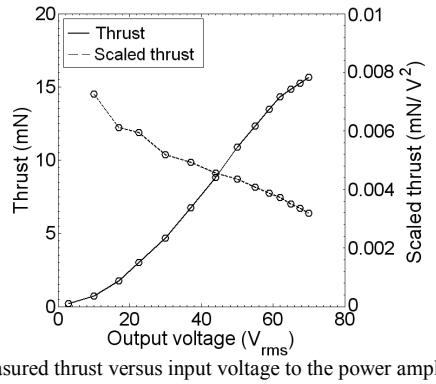

Figure 12. Measured thrust versus input voltage to the power amplifier using a 7MHz sinusoidal signal. Thrust increases with output voltage of the power amplifier to the UST, while scaled thrust has a decreasing trend. Data appear to saturate above $60V_{rms}$, which implies a disproportionate relationship.

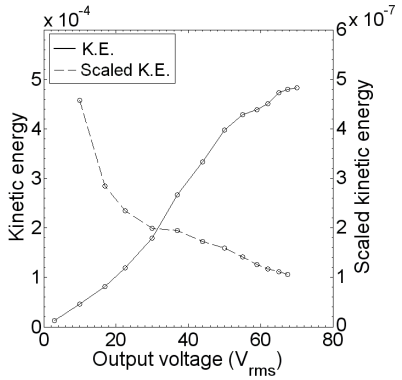

Figure 13. Total kinetic energy versus output voltage of the power amplifier using a 7MHz sinusoidal signal. Similar trends, as in thrust, can be seen for the kinetic energy and scaled kinetic energy when amplified voltage increases. Data appear to saturate above $55V_{rms}$, which also implies a disproportionate relationship

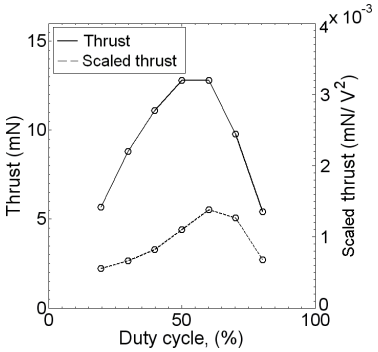

Figure 14. Thrust generated from a 7MHz square wave versus duty cycle. Thrust appears symmetrical about 50% duty cycle but the scaled thrust has an asymmetrical profile centering 60% duty cycle.

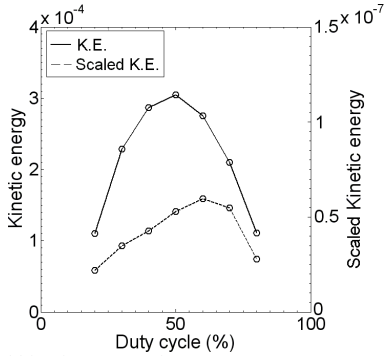

Figure 15. Total kinetic energy of a 7MHz square wave versus duty cycle. The *K.E.* appears symmetrical about 50% duty cycle but the scaled *K.E.* has an asymmetrical profile centering 60% duty cycle.

IV. UST DESIGN CONSIDERATIONS

A. Thrust and efficiency

To our knowledge, there are only two experimental works on ultrasonic propulsors reported; we compare them with our UST in terms of thrust density, scaled thrust and power density, in Table I. It is not clear if Allison [6], and Yu and Kim [16] tuned their devices to conditions of optimal performance, whereas our UST system was clearly operating at a resonance frequency. As such, it is difficult to make a fair and direct comparison of performance. We have employed a much higher power level, resulting in a very high thrust level and higher scaled thrust density. This latter property is important in applications because it indicates a very compact force source operating with reasonable voltage levels, exploitable to benefit from many of its unique ultrasonic attributes as discussed earlier in the introduction.

Fig. 16 details the acoustic efficiency of the UST operating with various waveforms, at 7MHz and with 50% duty cycle. This is based on (2): $T = \eta P/c$, where c is known (1480m/s), and P and T are measured. Both of the sinusoidal and the square waveforms lead to a "kinked" shape, with two straight portions relating thrust to electrical power; efficiency is calculated incrementally for each of the lines, that is, using the change in thrust versus the change in power. Below 70W electrical power, the power-thrust curve for sinusoidal input shows an acoustic efficiency of about 34%. Above 70 W, the UST efficiency falls to less than 10%. In general, the sinusoidal excitation is much more efficient than the square waveform. We note that the efficiency numbers given in Allison et al. [6] are somewhat higher than what we show here, in part because of their custom transducer design, but also because they operated at much lower power levels. Below 2mN, we also achieve high efficiency, around 70%. Other ultrasonic generators, such as the Capacitive Micro-machined Ultrasound Transducer (CMUT) [20], could be considered with respect to improving acoustic efficiency.

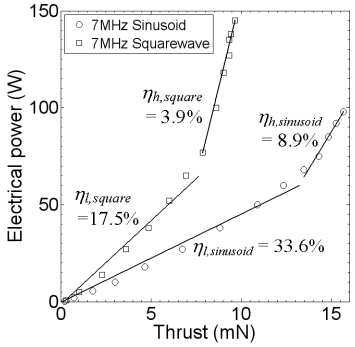

Figure 16. Electrical power driving the UST versus the thrust force produced. The *l* and *h* subscripts indicate evident low- and high-power regimes. The output voltage for the sinusoid is $59V_{rms}$, and for the square wave is $54V_{rms}$ at 50% duty cycle.

TABLE I
PERFORMANCE OF DIFFERENT UST DEVICES

Properties	Allison *et al.* [6]	Yu *et al.* [16]	This work
Frequency (MHz)	5.5	10.8	7.0
Voltage (V)	24.5	46	59
Electrical power (W)	5	--	69.5
Transducer surface area (mm^2)	$\pi/4\times10^2$	55	$\pi/4\times7^2$
Thrust (mN)	2.25	5.6	13.5
Thrust density (N/m^2)	28.6	224	350
Scaled thrust density ($N/m^2 \cdot V^2$)	0.05	0.11	0.10
Electrical power density (kW/m^2)	64	--	1806

B. Vehicular mission

In this subsection, we infer the expected speed and mission length that could reasonably be achieved from a UST-propelled underwater vehicle similar to *Huygens*. With the recorded images of *Huygens*, the advance speed measured is a constant 0.049m/s. The vehicle is quite streamlined, with only small holes around the frontal USTs, and a flat trim at the rear. From the top sectional view of *Huygens*, we can approximate the overall profile as an airfoil with a thickness-to-chord ratio of 0.37, and a span of 0.16m. The Reynolds number is $\mathrm{Re} = \frac{\rho U l_c}{\mu}$, where ρ (kg/m^3), U (m/s), l_c (m) and μ (kg/m·s) denote the fluid density, advance speed of the vehicle, chord length of the vehicle, and dynamic viscosity of the fluid respectively. The drag coefficient is $C_d = \frac{2T}{\rho A_w U^2}$, where T (N) and A_w (m^3) denote the thrust force, and wetted surface

area respectively. Expressing U on the left hand side of Re and C_d separately, the Reynolds number and drag coefficient can be related by

$$\mathrm{Re}^2 C_d = \frac{2\rho l_c^2 T}{A_w \mu^2}. \quad (8)$$

Using the Moody chart for a streamlined strut [21], U can then be estimated. To obtain the thrust, we recall that a sinusoidal input at 7MHz and 59Vrms, creates a thrust force of T = 13.5mN (Fig. 12). The constants ρ, l_c, A_w and μ are 1000kg/m^3, 0.215m, 0.053m^2, and 1.002×10^{-3}kg/m·s respectively. The parameter $\mathrm{Re}^2 C_d$, solved using (8), is 23.4×10^6, and for *Huygens*, a unique point can be identified on the $C_d - \mathrm{Re}$ Moody diagram; Re = 1.17×10^4 and $C_d = 0.17$. It is thus estimated that *Huygens* will advance at a velocity of 0.054m/s – very close to the observed value.

Regarding mission duration and length, a small 11V, 0.75Ah lithium-ion battery would occupy about 10% of the *Huygens* vehicle volume. We assume an average power capacity reduction of 90% in a single discharge cycle, providing about 7.4Wh of energy. The UST consumes 69W of electrical power with an acoustic efficiency of 33.6% (Fig. 16), to produce 13.5mN of thrust with a constant vehicle advance velocity of about 0.05m/s. If we assume the instrumentation and other loads are small compared to the propulsive load, a simple straight-path mission will last around six minutes and travel a distance of about twenty meters. A somewhat larger battery could power the vehicle for perhaps thirty minutes, with a mission length of one hundred meters. While the UST is clearly not competitive with rotary or some biomimetic propulsors in terms of transit efficiency, nonetheless these estimates show that maneuvering a very small-scale vehicle utilizing USTs could be practical with or without a power tether. New applications, designed to exploit the UST's unique attributes, will certainly find this technology an indispensable solution.

V. Conclusions

We believe that ultrasonic thruster technology can bring important and novel attributes to marine robotic devices and systems. These include low cost and high robustness when applied at the centimeter scale or smaller. The robustness is due to the fact that the UST effectively has no moving parts, and will not biofoul – these are properties unavailable in the rotary and biomimetic propulsors in use today. Experiments here and in other references indicate that waveform, frequency, and voltage level can all strongly influence the behavior of the UST, in terms of wake, thrust, and efficiency. We have successfully implemented three sub-centimeter UST devices into a small robot, and made preliminary calculations showing that viable, maneuvering-intensive missions can be developed with such craft, despite its inherently low propulsive efficiency.

Clearly UST technology would benefit from further developmental work on application-specific components. We can envision vehicles carrying USTs that double as short-range acoustic communication elements, or as a self-cleaning inspection sonar. Aside from the possibilities mentioned relating to the thrust-wake independence, it may be possible to pre-distort a source waveform so as to maintain a constant streaming flow while separately controlling thrust, or to "over-distort" a source signal to achieve maximum flow without a significant variation in thrust. The UST could complement an existing propulsor to provide maneuvering, or to strategically control or manipulate a flow-field for other purposes. Propulsive efficiency could conceivably be enhanced by developing a waveguide external to the transducer. We established in [10] a direct connection between UST thrust and the wake velocity profile; such analyses give a richer understanding of design choices. With improvements along these lines, the UST could well become an important enabler for very small marine vehicles, and might find use in other completely separate applications.

Acknowledgment

We are grateful to M. Triantafyllou and B. Simpson for access to a PIV system.

References

[1] W. Trimmer and R. Jebens, "Actuators for micro robots," in *Proceedings. 1989 IEEE International Conference on Robotics and Automation (Cat. No.89CH2750-8), 14-19 May 1989*, Washington, DC, USA, 1989, pp. 1547-52.

[2] K. L. Doty, *et al.*, "An autonomous micro-submarine swarm and miniature submarine delivery system concept," in *Florida Conference on Recent Advances in Robotics*, Florida, 1998, pp. 131-138.

[3] C. E. Wick and D. J. Stilwell, "USNA-1: A miniature, low-cost autonomous underwater vehicle: Designed to support one-way missions and provide an academic platform for navigation, sensor and AUV employment research," *Sea Technology,* vol. 43, pp. 17-25, Jun. 2002 2002.

[4] N. Kottege and U. R. Zimmer, "Acoustical localization in schools of submersibles," in *OCEANS 2006 - Asia Pacific, 16-19 May 2006*, Piscataway, NJ, USA, 2007, pp. 573-7.

[5] B. Watson, *et al.*, "Piezoelectric ultrasonic resonant micromotor with a volume of less than 1 mm3 for use in medical microbots," in *2009 IEEE International Conference on Robotics and Automation (ICRA), 12-17 May 2009*, Piscataway, NJ, USA, 2009, pp. 2225-30.

[6] E. M. Allison, *et al.*, "Ultrasonic propulsion," *Journal of Propulsion and Power,* vol. 24, pp. 547-553, 2008.

[7] D. T. Blackstock, *Fundamentals of physical acoustics*: New York : Wiley, 2000.

[8] J. Lighthill, "Acoustic streaming," *Journal of Sound and Vibration,* vol. 61, pp. 391-418, 1978.

[9] O. V. Rudenko and S. I. Soluian, "Theoretical foundations of nonlinear acoustics," p. 274, 1977.

[10] A. C. H. Tan and F. S. Hover, "Correlating the ultrasonic thrust force with acoustic streaming velocity," in *2009 IEEE International Ultrasonics Symposium, IUS 2009, September 20, 2009 - September 23, 2009*, Rome, Italy, 2009, pp. 2627-2630.

[11] M. F. Hamilton and D. T. Blackstock, *Nonlinear acoustics* Academic Press, 1998.

[12] H. Mitome*, et al.*, "Effects of nonlinearity in development of acoustic streaming," *Japanese Journal of Applied Physics, Part 1 (Regular Papers & Short Notes),* vol. 34, pp. 2584-9, 1995.

[13] J. Wu and G. Du, "Acoustic streaming generated by a focused Gaussian beam and finite amplitude tonebursts," *Ultrasound in Medicine and Biology,* vol. 19, pp. 167-176, 1993.

[14] H. C. Starritt*, et al.*, "An experimental investigation of streaming in pulsed diagnostic ultrasound beams," *Ultrasound in Medicine & Biology,* vol. 15, pp. 363-73, 1989.

[15] A. C. H. Tan and F. S. Hover, "On the influence of transducer heating in underwater ultrasonic thrusters," in *the 20th International Congress on Acoustics* Sydney, Australia, 2010.

[16] H. Yu and E. S. Kim, "Ultrasonic underwater thruster," in *17th IEEE International Conference on Micro Electro Mechanical Systems (MEMS): Maastricht MEMS 2004 Technical Digest, January 25, 2004 - January 29, 2004*, Maastricht, Netherlands, 2004, pp. 486-489.

[17] M. R. Myers*, et al.*, "Direct methods for characterizing high-intensity focused ultrasound transducers using acoustic streaming," *Journal of the Acoustical Society of America,* vol. 124, pp. 1790-1802, 2008.

[18] B.-G. Loh and D.-R. Lee, "Heat transfer characteristics of acoustic streaming by longitudinal ultrasonic vibration," *Journal of Thermophysics and Heat Transfer,* vol. 18, pp. 94-99, 2004.

[19] T. Kamakura*, et al.*, "Time evolution of acoustic streaming from a planar ultrasound source," *Journal of the Acoustical Society of America,* vol. 100, pp. 132-132, 1996.

[20] B. Bayram*, et al.*, "Capacitive micromachined ultrasonic transducer design for high power transmission," *IEEE Transactions on Ultrasonics, Ferroelectrics, and Frequency Control,* vol. 52, pp. 326-338, 2005.

[21] S. F. Hoerner, *Fluid-dynamic drag: practical information on aerodynamic drag and hydrodynamic resistance*: Midland Park, N. J., 1965.